PCCP

PAPER

View Article Online
View Journal

Cite this: DOI: 10.1039/d6cp00309e

Role of structural isomerism in the properties of imine-based organic hole-transporting materials

Benjamin Vella,†[a] Dylan Wilkinson, ‡[a] Son Singh,[b] Stephen Sproules,[a] Soad S. Alzahrani,[c] Abdulrahman G. Alhamzani,[c] Abdul-Wasir Shaka,[a] Shahzada Ahmad,[bdef] Sondos A. J. Almahmoud,*[c] Graeme Cooke*[a] and Pablo Docampo§*[a]

Organic hole-transporting materials (HTMs) play a key role in enhancing both the efficiency and endurance of photovoltaic devices and for optoelectronic applications. In contrast to their inorganic counterparts, they offer distinct advantages such as solution processability, tunable properties, and low-cost fabrication. However, their electrical conductivity in most cases is intrinsically low and can be enhanced through doping using chemical oxidants. Doping typically involves the partial oxidation of the HTM, generating additional free charges and improved film conductivity. In this work, we investigate the effect of molecular design on the doping mechanism, with a specific focus on imine-linked, triarylamine-based compounds. Our research indicates that the effectiveness of doping and resulting conductivity are determined by the energy of the dopant–HTM complex. Through a combined approach including density functional theory (DFT) modelling, spectroscopy, and conductivity measurements, we observe that oxidation of the HTM does not guarantee doping if the generated charges are not free. This highlights the importance of imine bond orientation in the stabilisation of generated holes. Interestingly, a seemingly trivial chemical change, such as the inversion of an imine bond affects the doping of the material. Our findings show that such isomerisation can result in charge transfer complexes with stabilised holes that do not improve conductivity. This challenges many common approaches to chemical doping, where standard additives are added to newly developed HTMs without prior investigation of their efficacy for the chemical system being studied. We advocate for a tailored understanding of the doping mechanism and the use of spectroscopic techniques to enhance HTM design and characterisation.

Received 28th January 2026,
Accepted 12th May 2026

DOI: 10.1039/d6cp00309e

rsc.li/pccp

Introduction

Hole-transporting materials (HTMs) play an essential role in various optoelectronic devices, particularly in perovskite solar cells (PSCs), solid-state dye-sensitised solar cells (ss-DSSC), and organic light-emitting diodes (OLEDs). These materials are responsible for the effective transfer of positive charge carriers, known as holes, from the active layer to the electrodes, which significantly improves both the efficiency and stability of the devices.[1,2] The use of HTMs composed of semiconducting small organic molecules and polymers has become a prominent area of research in the field of optoelectronic devices. This is attributed to the advantages that organic HTMs offer compared to their inorganic counterparts, including the abundance of raw materials, low-cost, flexibility of molecular design, excellent solubility, environmental sustainability, solution-processability, mechanical flexibility, tunability of electronic properties, good film-forming characteristics, and ease of fabrication.[2–4]

Since the main functions of HTMs are to transport holes to electrodes for collection and block the opposite charges

[a] School of Chemistry, University of Glasgow, University Avenue, Glasgow, G12 8QQ, UK. E-mail: Graeme.Cooke@glasgow.ac.uk, pablo.docampo@bcmaterials.net
[b] BCMaterials, Basque Center for Materials, Applications, and Nanostructures, UPV/EHU Science Park, 48940 Leioa, Spain
[c] Department of Chemistry, College of Science, Imam Mohammad Ibn Saud Islamic University (IMSIU), Riyadh 11623, Saudi Arabia. E-mail: salmahmoud@imamu.edu.sa
[d] IKERBASQUE, Basque Foundation for Science, Bilbao 48009, Spain
[e] New Energy & Optical Materials Lab., Departament de Química Inorgànica i Orgànica and Institut de Química Teòrica i Computacional, Diagonal 645, Universitat de Barcelona, E-08028, Spain
[f] Institució Catalana de Recerca i Estudis Avançats (ICREA), Barcelona, Spain
† Current address: Strathclyde Institute of Pharmacy and Biomedical Sciences, University of Strathclyde, Glasgow, G4 0RE, UK.
‡ Current address: RIKEN Center for Emergent Matter Science (CEMS), 2-1 Hirosawa, Wako, Saitama 351-0198, Japan.
§ Current address: BCMaterials, Basque Center for Materials, Applications, and Nanostructures, UPV/EHU Science Park, 48940, Leioa, Spain.

(electrons), HTMs need to exhibit certain advantageous characteristics. These include high hole mobility, the ability to form morphologically stable thin films, a highest occupied molecular orbital (HOMO) level with optimal energy alignment that facilitates a low energy barrier for hole injection from the active layer into the anode, and a well-defined lowest unoccupied molecular orbital (LUMO) level that prevents electron injection from the active layer into the hole transport layer.[2,4,5] A high glass transition temperature (T_g) is also a critical parameter in the development of reliable HTMs to prevent their crystallisation after heating above their T_g, thus providing thermal and morphological stability.[6] For organic HTM synthesis, specific molecular design needs to be considered, commonly, it incorporates aromatic conjugated systems with electron-donating moieties such as triphenylamine (TPA) and carbazole, due to their desirable characteristics of high charge carrier mobility and reduced ionisation potential (IP).[2]

Many highly efficient HTMs have been developed, including the state-of-the-art 2,2′,7,7′-tetrakis(*N*,*N*-di-4-methoxyphenyl)amino-9,9′-spirobifluorene (Spiro-OMeTAD). Spiro-OMeTAD is by far the most studied example, which displays a HOMO of ~4.9 eV and a hole mobility of $\sim 2 \times 10^{-4}$ cm^2 V^{-1} s^{-1}.[7–10] The spiro-linked compounds, exhibit a high T_g value, ensuring morphological stability and facilitating ease of processing, while maintaining favourable electronic properties.[6] Although spiro-OMeTAD is the most widely explored HTM and allows for high power conversion efficiencies (PCEs) in devices, several drawbacks spurred researchers to develop different HTMs. Spiro-like HTMs require a complex and multi-step synthesis process, coupled with challenges in purification which significantly limit their feasibility for large-scale application as HTMs in optoelectronic devices.[10]

Moreover, Spiro-OMeTAD not only suffers from high production costs due to its complex synthesis and purification requirements but also exhibits poor hole mobility ($\mu_h \sim 10^{-4}$ cm^2 V^{-1} s^{-1}). This low mobility leads to increased recombination losses, which is a major drawback for its use in various applications, particularly in PSCs.[10] This led the attention towards developing alternative HTMs to spiro-OMeTAD with low cost and high efficiency.[11–14] Although a wide range of HTMs has been proposed as alternatives to spiro-OMeTAD, only very few examples have resulted in μ_h values that are comparable to those exhibited by spiro-OMeTAD.[12,13,15]

High-performing HTMs are generally synthesised *via* cross-coupling reactions.[16–21] Specific conditions such as inert atmosphere, expensive catalysts, and extensive product purification are necessary for these reactions, which ultimately lead to high costs and limit large-scale commercialisation. Consequently, derivatives of triphenylamine-based HTMs were synthesised through catalyst-free methods, employing aryl halides and aldehydes as precursors. This approach facilitated the introduction of diverse HTMs featuring olefin, amide, or imine linkages that connect the electron-donating units.[14,22–27] A series of HTMs have previously been synthesised *via* simple and clean Schiff-base condensation chemistry with an estimated material cost in the range of 4–54 $ per g.[27] The Schiff-base condensation reaction offers several advantages, as it can be performed under mild conditions without the need for expensive catalysts. This results in a straightforward product purification process involving only water as a byproduct, which can be easily removed, avoiding the formation of side products that can result from the use of transition metal catalysts.[27,28]

We have recently introduced a range of HTMs for PSCs that are synthesised using Schiff-base condensation chemistry. These compounds predominantly contain the imine group (C═N), which is typically formed through a simple condensation reaction between an active carbonyl compound and a primary amine. The materials showed increased conductivity of up to 10^{-3} S cm^{-1} after doping with LiTFSI, and hole mobilities of up to 10^{-5} cm^2 V^{-1} s^{-1}, comparable to those of well-known state-of-the-art HTMs such as Spiro-OMeTAD.[27] The effects of inverting the imine bond orientation was also performed in order to examine the impact of the nitrogen position in the π-bridged linker moiety.[27]

Devices using isomeric imine HTMs showed significant differences in the bandgap of the materials and a significant decrease in PCE when the imine nitrogen is oriented towards the core as opposed to the TPA arms. This was attributed to a significantly reduced HOMO energy for this HTM. The difference in HOMO energy levels was thought to introduce a hole injection barrier at the perovskite interface, resulting in high series resistance that restricted the short-circuit current (J_{sc}) of the device. Nevertheless, the largest reported changes in HOMO energies calculated from DFT or estimated as IPs from cyclic voltammetry (CV) between the two HTMs in Fig. 1 were only

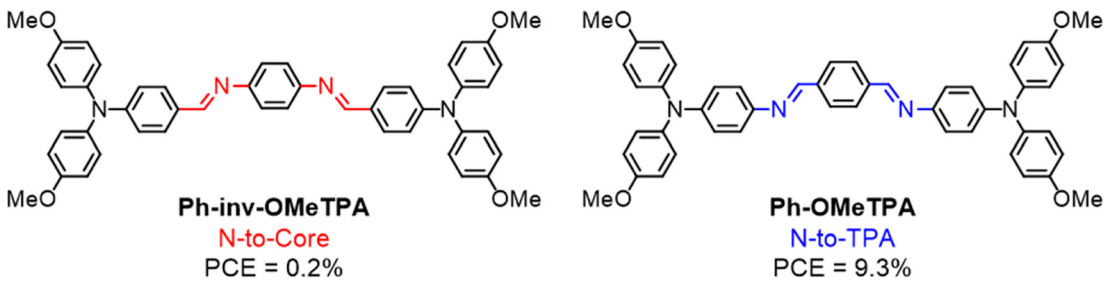

Fig. 1 Two isomeric imine structures studied in Petrus, *et al.* (2017). The two symmetrical imine bond orientations are illustrated, along with the drastically reduced PCE for the N-to-core orientation compared to N-to-TPA.[27]

around 0.1 eV. A significant decrease in conductivity between the two HTMs was noted after doping, with a tenfold decrease in conductivity for the N-to-core (1×10^{-7} S cm^{-1}) orientation compared to N-to-TPA (5×10^{-6} S cm^{-1}) at the same doping level (Fig. 1).[27] This indicates that variations in the oxidation and doping processes of the two HTMs are likely responsible for the observed difference in PCE, emphasising that a small change in the molecular design can significantly affect the overall performance.

Huang and co-workers found that reversing imine bond orientations in covalent organic frameworks (COFs) featuring bipyridine cores results in significant disparities in their physical properties, photophysical characteristics, and photocatalytic efficiency for CO_2 reduction. This stems from the polarisation characteristics of the imine bond facilitating a preferential orientation for intramolecular charge transfer (ICT) upon photoexcitation.[29] It was also found that when the imine nitrogen is not bonded directly to the core, the bipyridine functioned as an electron acceptor, generating a delocalised hole with a localised electron. When the imine orientation was reversed, the bipyridine functioned as an electron donor and displayed the opposite functionality, generating a delocalised electron with a localised hole.[29] Nevertheless, there is still a lack of essential research on how the orientation of the imine bond impacts the reaction between the HTM and the chemical additives used in the fabrication of optoelectronic devices. Here, we investigate the effect of the orientation of the imine bond on oxidation mechanisms and conductivity of imine-based HTMs.

This investigation is conducted on two novel imine materials, **BiPh-inv-OMeTPA** (**10**) and **BiPh-OMeTPA** (**12**) (Scheme 1), comprised of biphenyl cores with TPA sidearms. The biphenyl moiety represents another simple and readily available building block that appears in many HTM structures found in the literature, where it is often attached to the rest of the HTM molecule through C–C bonds formed by cross-coupling reactions such as the Suzuki couplings.[21,30,31] This results in the same drawbacks inherent in the synthesis of Spiro-OMeTAD. We introduce the imine bond as a linker between the biphenyl core and the TPA moieties, which greatly simplifies the synthesis of the target compounds due to the abundance of commercially available functionalised biphenyls and easy synthesis of functionalised triphenylamines. The all-aromatic nature of the compounds allows for conjugation of the imine bonds, improving their resistance to aqueous hydrolysis which commonly affects the stability of imine groups. Furthermore, the large number of phenyl rings in the structure can present additional opportunities for π–π stacking, which can improve the lifetime of a charge-separated excited state, leading to enhanced electrical properties.[32,33] The orientation of the nitrogen atom in the imine bond was found to have a significant effect on the resulting film conductivity and photovoltaic performance. Significant differences in electron density distribution and oxidation behaviour between the two orientations are revealed from DFT and spectroscopic studies.

Results and discussion

Synthesis

The two imine-based HTMs were synthesised as shown in Scheme 1. The materials involved functionalised TPA sidearms coupled to a conjugated biphenyl core, with the imine bond attached in two opposing orientations. In compound **12**, the nitrogen is bonded to the TPA donor arms, while for compound **10** the nitrogen is bonded to the biphenyl core. All target HTMs were synthesised through Schiff-base condensation reactions, involving simple and cheap building blocks that were either easy to prepare (**3**, **4**, **6**, **7**, **9**) or commercially available (**1**, **2**, **5**, **8**, **11**). Imine-based HTMs are obtained in 43% and 49% yield for compounds **10** and **12**, respectively. To study the influence of the imine bond orientation on the doping mechanism and redox properties of imine-based HTMs, four additional model compounds (**14**, **15**, **17**, **18**) were also synthesised using condensation chemistry with similarly mild conditions (Scheme 2). Target compounds were characterised by ^{1}H NMR, ^{13}C NMR and mass spectrometry. The ^{1}H NMR spectra recorded for intermediates **3**, **4**, **6**, **7**, and **9** agree with previous reports in the literature.[24,36–38]

DFT modelling

The target HTMs **10** and **12**, as well as the model compounds **14**, **15**, **17**, and **18** were investigated using DFT calculations using Gaussian 09 software to study the influence of the imine bond orientation on the structural and electronic properties of the compounds (Fig. 2). All molecular structures were geometrically optimised using the hybrid B3LYP functional and a 6-311G** basis set. HOMO and LUMO energies were calculated from the optimised structures. Frequency calculations were performed, to confirm the absence of a transition state. The HOMO for compound **10** is found to be localised over the entire molecule, while for compound **12** the HOMO is mainly localised on the TPA moiety. In the case of LUMO levels, the electron density distribution is mainly localised over the central core (*i.e.*, biphenyl) for both HTMs. Therefore, the extent of overlap between HOMO and LUMO is lower for compound **12** compared to the inverted imine derivative compound **10**. Compound **10** has a wider band gap (E_g) of 3.25 eV compared to 2.65 eV for compound **12**. This can be attributed to the significant change in both HOMO and LUMO levels of compound **10** upon inversion of the imine group. The TPA model compounds **14** and **17** both have the HOMO located on the TPA moiety with the LUMO centred around the imine bond, delocalised over the phenyl rings on either side. The biphenyl model compounds **15** and **18** both possess HOMO and LUMO delocalisation over the whole molecule. The effect of imine bond isomerisation is less pronounced on the model compounds and affects the target molecules **10** and **12** to a greater extent.

The impact of the electronegative nitrogen atoms and their orientation in the imine bond affects the electron density distribution throughout the molecule. This was visualised using electrostatic potential (ESP) maps, which were computed

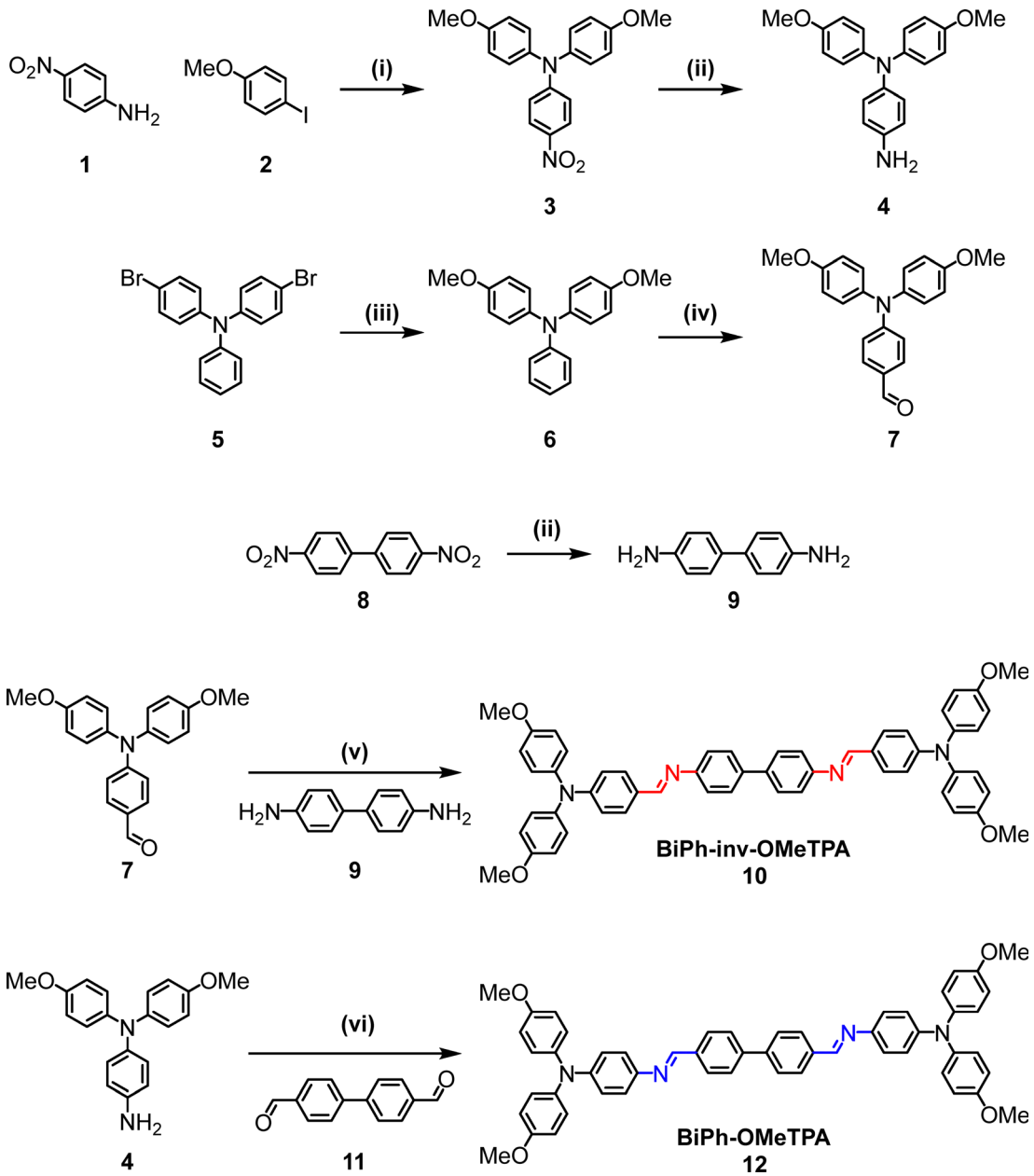

Scheme 1 Synthesis of imine HTMs. Conditions: (i) K_2CO_3, copper powder, 18-crown-6, DMF, reflux (150 °C, 16 hours), yield 67%; (ii) 10% palladium on carbon, hydrazine hydrate, dry THF, reflux (66 °C, 16 hours); (iii) sodium metal, methanol, 0 °C then copper(I) iodide, DMF, 90 °C, 12 hours; (iv) $POCl_3$, DMF, 0 °C, then 90 °C for 12 hours; (v) $MgSO_4$, p-TsOH, EtOH, 80 °C, 16 hours, (vi) $MgSO_4$, p-TsOH, EtOH, 25 °C, 16 hours.

for compounds **10**, **12**, **14**, **15**, **17**, and **18** (Fig. 3). In compound **10**, the biphenyl core is much more electron-rich compared to compound **12** since it is directly bonded to the nitrogen atom of the imine bond. The nitrogen atoms in the imine bond facilitate the movement of electron density towards the respective moieties they are connected to, directing electron density towards the core in compound **10** and towards the TPA arms in compound **12**. A similar effect is seen for all model compounds as well, where electron density is concentrated on the phenyl rings directly bonded to the imine nitrogen atom.

Optical and electrochemical properties

Since HTMs need to transport charges effectively to their respective electrodes, appropriate alignment of energy levels is required. Therefore, optical and electrochemical studies of the HTMs were performed to gain insights into these parameters. UV-Visible absorption and emission spectra of compounds **10** and **12** are summarised in Fig. 4 and Table 1. Compound **10** showed a maximum absorption λ_{max} at 402 nm, while compound **12** showed a 20 nm bathochromic shift with λ_{max} at 422 nm. The bathochromic shift associated with switching between the two imine bond orientations results in a reduced

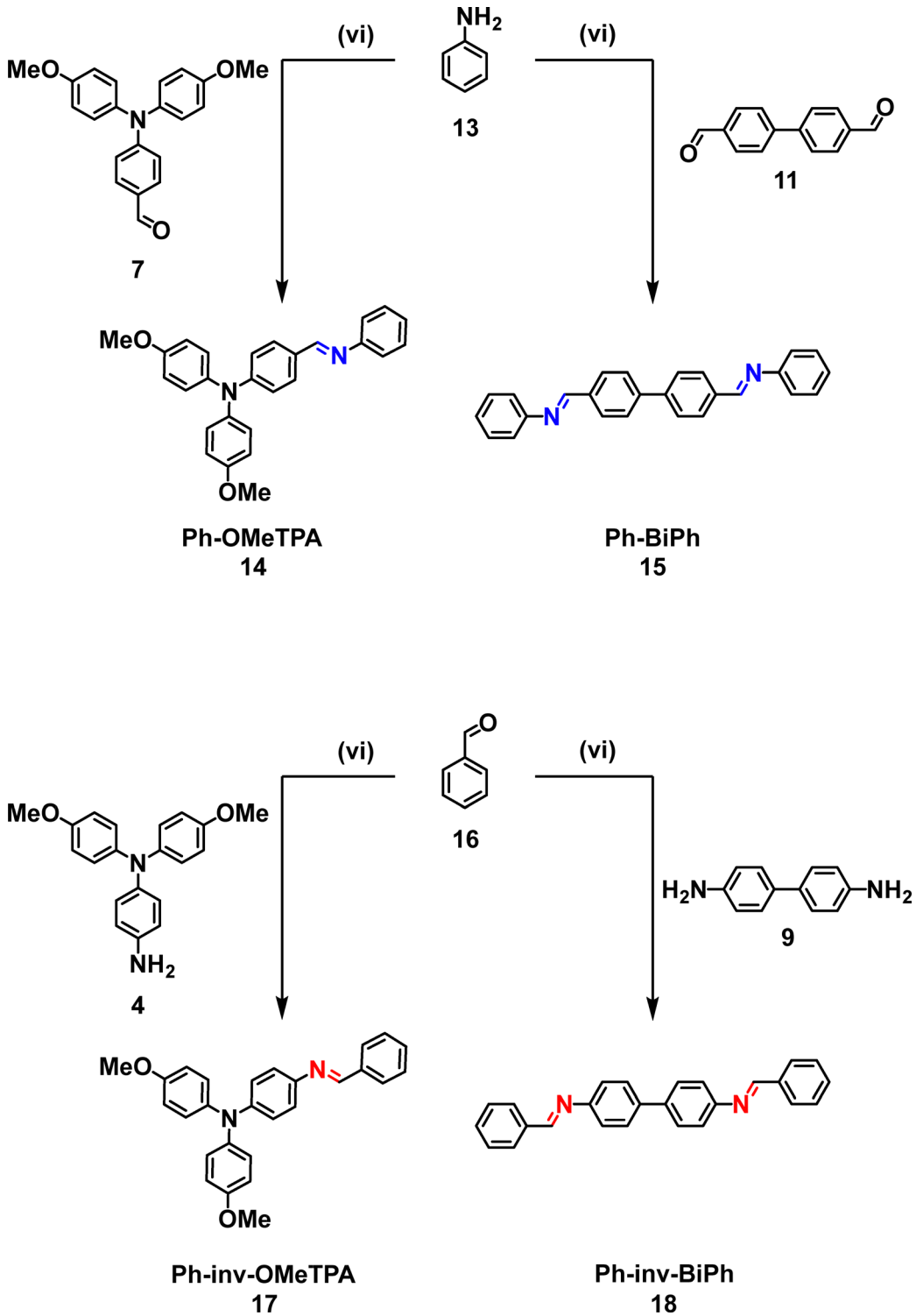

Scheme 2 Synthesis of four imine model compounds. Conditions: (vi) $MgSO_4$, p-TsOH, EtOH, 25 °C, 16 hours.

optical gap (E_{opt}) for compound **12**, which might indicate potential variations in planarity and, hence, conjugation across the entire molecule.

We estimated the E_{opt} for both HTMs **10** and **12** using Tauc plots (Fig. 4b and c). Compound **12** showed a reduced E_{opt} of 2.63 eV compared to compound **10**, which gave an E_{opt} of 2.79 eV. These findings are consistent with previously reported studies.[27,39] The emission spectra show that compound **10** fluoresces at a longer wavelength (544 nm) compared to compound **12** (481 nm), with Stokes shifts of 142 nm (70 423 cm^{-1}) and 57 nm (175 439 cm^{-1}) for **10** and **12**, respectively. This indicates a greater degree of flexibility in

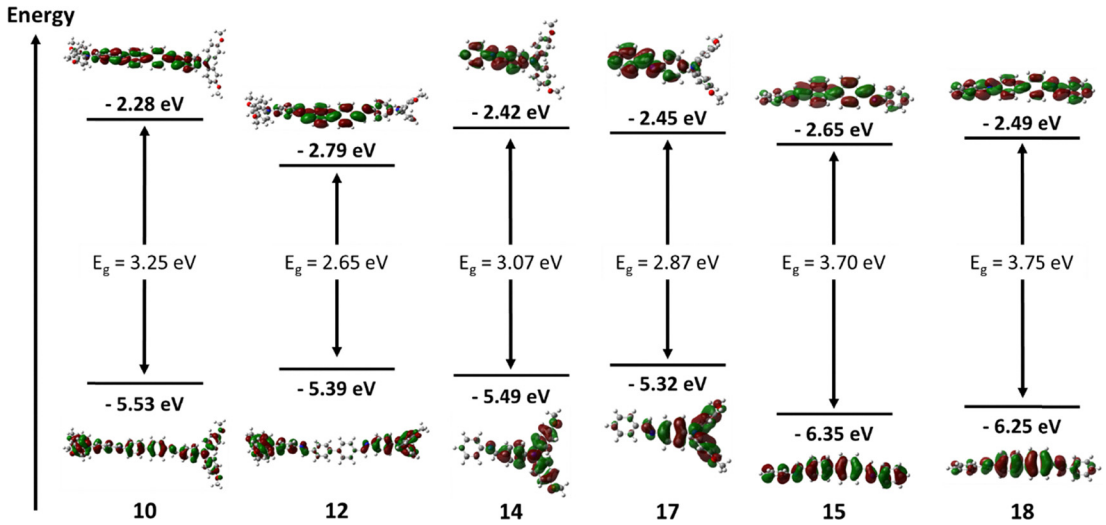

Fig. 2 Molecular orbital distribution of HTMs **10** and **12**, as well as model compounds **14**, **15**, **17**, and **18** calculated at B3LYP 6-311G** level.

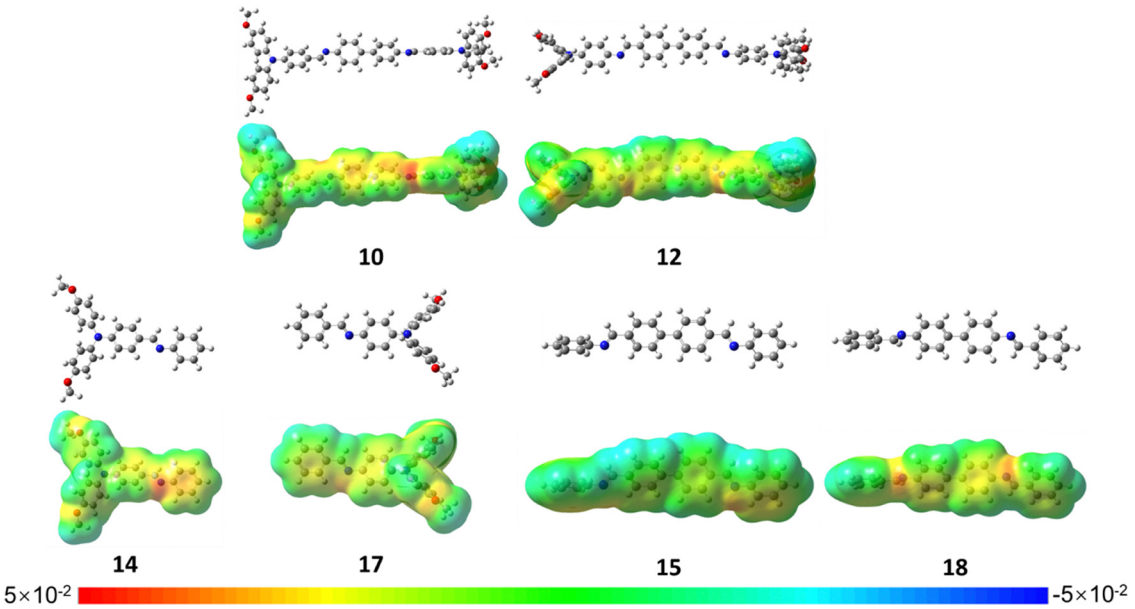

Fig. 3 Optimised geometries and ESP maps of HTMs **10** and **12** and model compounds **14**, **15**, **16**, and **17** at the B3LYP 6-311G** level.

the molecule and more significant structural changes upon light excitation.[16,40]

To gain insight into the IP and electron affinity (EA) of the target HTMs, cyclic voltammetry (CV) and square wave voltammetry (SWV) measurements were performed using 10^{-4} M solutions of the target compound in dimethylformamide (DMF) as solvent. All voltammograms were referenced to the Fc/Fc$^+$ redox couple (Fig. 5 and Table 1). The results show that changing the imine bond orientation results in differences in the oxidation profile of the HTMs. Compound **10** shows a higher IP of 5.27 eV compared to that of compound **12** (5.04 eV). Furthermore, an irreversible oxidation was observed at approximately 0.05 V for compound **10**, which was not seen in the square-wave voltammogram (Fig. 5b). This irreversible oxidation may indicate an irreversible side reaction taking place during the oxidation process. It may also result from the precipitation of the oxidised product, which may contribute to the irreversible wave. In order for the HTM to perform effectively, the oxidation process must be reversible to facilitate the conductivity that is dependent on redox reactions occurring between radical cations and neutral molecules to transfer charge through the HTM layer.[41] In compound **10**, the imine bond orientation may result in electron density being localised on the biphenyl moiety, increasing the likelihood of removing an electron from the core rather than from the TPA sidearm. Hence, the irreversible oxidation might result in a permanent chemical change within the molecule which, in turn, prevents the generation of a mobile hole. This aligns with the findings from the DFT studies (Fig. 2).

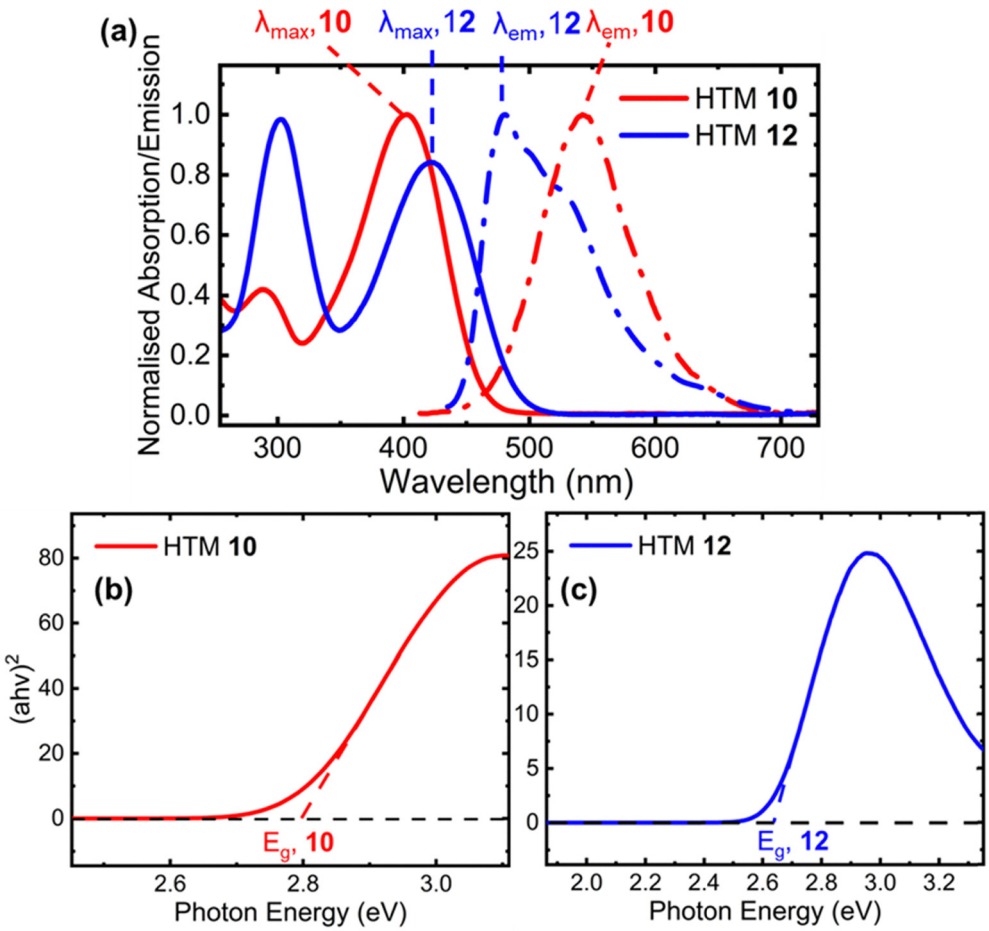

Fig. 4 (a) UV-Visible absorption and emission properties of HTMs **10** and **12**, measured in dichloromethane from 10^{-5} M solutions. (b) and (c) Tauc plots prepared from their UV-visible absorption spectrum.

Table 1 Optical and electrochemical properties of HTMs **10** and **12**, as well as model compounds **14**, **15**, **17**, **18**

Compound	λ_{max} (nm)	E_{opt} (eV)	$E_{1/2}$ *vs.* Fc^+/Fc (V)	IP (eV)
10	402	2.79	0.47	5.27
12	422	2.63	0.24	5.04
14	461	2.81	0.25	5.05
15	342	3.19	−0.18	4.62
17	396	2.76	0.33	5.13
18	351	3.10	−0.12	4.69

To further investigate whether the imine orientation is responsible for the observed irreversible oxidation of compound **10** and further understand the redox properties of compounds **10** and **12**, CV and SWV experiments were also performed on the four model compounds. The voltammograms are depicted in Fig. 7, and all estimated IPs are summarised in Table 1. In Fig. 6a, models **18** and **15** based on biphenyl core show IPs of 4.69 eV and 4.62 eV, respectively. They also exhibit comparable irreversible characteristics at 0.25 V to those in the parent HTM **10**. This implies that the irreversibility oxidation is due to the biphenyl core of the HTM, rather than the TPA sidearms. Furthermore, the inversion of the imine bond orientation in compound **12** enhances the electrochemical reversibility of the system. In compound **12**, the TPA sidearm undergoes reversible oxidation, while in compound **10**, the biphenyl core is the first to undergo irreversible oxidation. The DFT studies suggest that the HOMO of compound **10** can potentially delocalise across the whole molecule, causing the biphenyl core to oxidise when exposed to a chemical oxidant.

Similar behaviour to compound **10** was observed for compounds **17** and **18**, while compounds **14** and **15** show reversible oxidation to the TPA sidearm. One can conclude that the IPs of these HTMs appear to be influenced by both their molecular structure and the orientation of their imine bonds. Compounds **10**, **17**, and **18** generally exhibit higher IPs, while compounds **12**, **14**, and **15** tend to have lower IPs.

This trend suggests that imine bonds oriented towards the biphenyl core may contribute to higher stability against oxidation, potentially attributable to increased electron delocalisation or variations in the electronic distribution within the molecule, which is in agreement with the DFT studies. On the other hand, the opposite imine orientation appears to promote more efficient oxidation, potentially offering advantages for hole injection or extraction in certain device architectures. This orientation-specific behaviour presents a crucial design principle for modifying the electronic

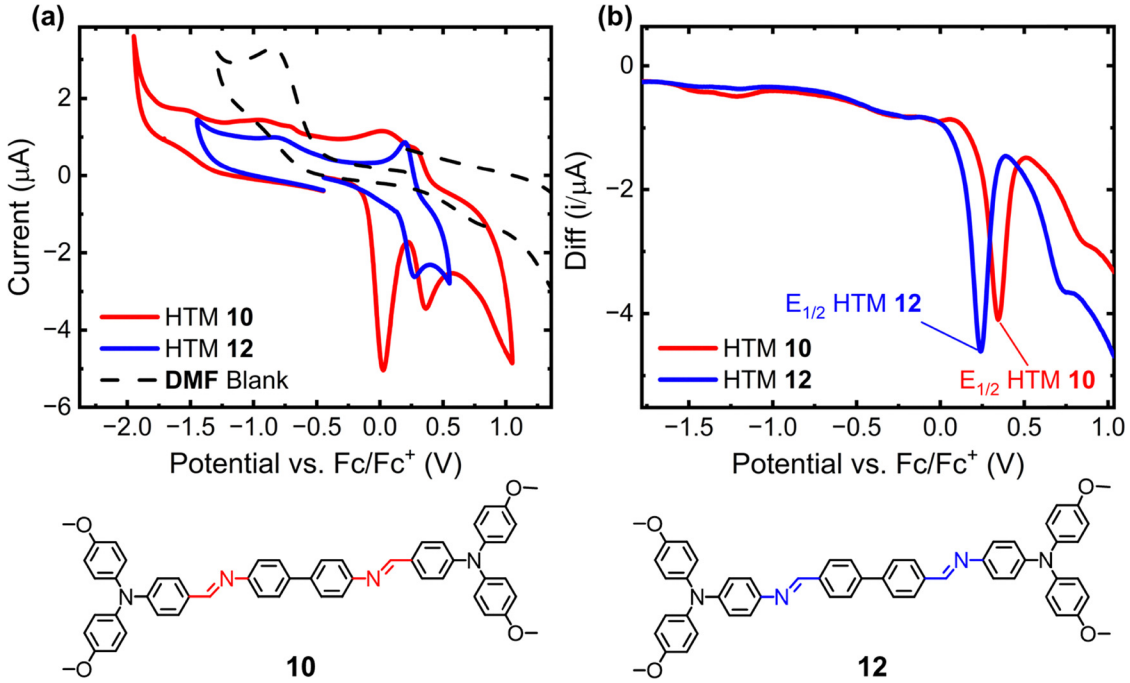

Fig. 5 (a) Cyclic voltammograms and (b) square-wave voltammograms recorded from 10^{-4} M solutions in DMF for HTMs **10** and **12**.

properties of HTMs for specific applications in optoelectronic devices.

Thermal properties

The thermal properties of compounds **10** and **12** were analysed using thermogravimetric analysis (TGA) and differential scanning calorimetry (DSC), and results are shown in Fig. 7. It is of great importance to study the thermal stability of any HTMs to ensure their feasibility in photovoltaic systems that function in high temperatures. In this case, maintaining the stability of the amorphous state is crucial for achieving strong interfacial contact. Conjugated imines have been found to possess good thermal stability, making them appropriate for such applications.[34,35] Fig. 8 shows the similar thermal stability between the two HTMs.

In the thermograms shown in Fig. 7a, an initial mass loss of 5% is seen for HTM **10** from 110–180 °C. A plateau is observed after this point, suggesting that the observed changes do not stem from decomposition but instead reflect a mass loss of a different nature. We exclude the evaporation of solvent due to the sample being extensively dried under vacuum for several hours before the measurement. An identical TGA trace was recorded after drying compound **10** for a further 12 hours under vacuum, which verifies that residual solvent is not responsible for the original mass loss (SI, Fig. S13). Full decomposition was recorded for both HTMs at around 400 °C, thus confirming the excellent stability of the imine materials towards thermal decomposition. HTM **12** exhibits a glass transition T_g = 75 °C, which is typically undesirable for solar cell applications as it may lead to low morphological stability of the HTM under normal operation.[42] At higher temperatures, both HTMs exhibit exothermic transitions at 137 °C (compound **12**) and 205 °C (compound **10**) due to crystallisation or aggregation in the solid state. A further melting transition is seen for HTM **12** at 175 °C. Interestingly, compound **10** does not exhibit glass transitions or melting in the DSC, highlighting the significant difference in thermal character between the isomeric imine molecules.

FTIR spectroscopy

ATR-FTIR was used to investigate the molecular structure of compounds **10** and **12**. As illustrated in Fig. 8, the presence of low-intensity bands above 3000 cm^{-1} is associated with aromatic ν_{C-H} stretching modes. The peaks around 2950, 2832 cm^{-1} (compound **10**) and 2933, 2829 cm^{-1} (compound **12**) correspond to the stretching vibrations of methyl groups. The characteristic band of the imine group, $\nu_{C=N}$ is observed at about 1584 cm^{-1} in the case of compound **10** and at about 1617 cm^{-1} for compound **12**. The aromatic $\nu_{C=C}$ stretching modes are found between 1600 and 1500 cm^{-1}, overlapping with the imine stretching band. The bands at 1236 and 1157 cm^{-1} correspond to ν_{C-O} stretching modes for compounds **10** and **12**, respectively. Additionally, both compounds exhibit the in-plane aromatic bending mode δ_{CH} at 1031 cm^{-1} (**10**) and 1033 cm^{-1} (**12**). For compound **10**, the out-of-plane bending modes are detected at 822, 781, and 721 cm^{-1}, and for compound **12** at 826, 781, and 718 cm^{-1}. The imine stretching band in compound **10** appears at a lower wavenumber than that of compound **12**. This might indicate that compound **10** possesses a higher conjugation in its ground state than compound **12**. This result aligns with DFT predictions (Fig. 2), where the HOMO for compound **10** is found to be delocalised over the entire molecule, suggesting a higher conjugation between the triphenylamine units and the core compared to compound **12**.

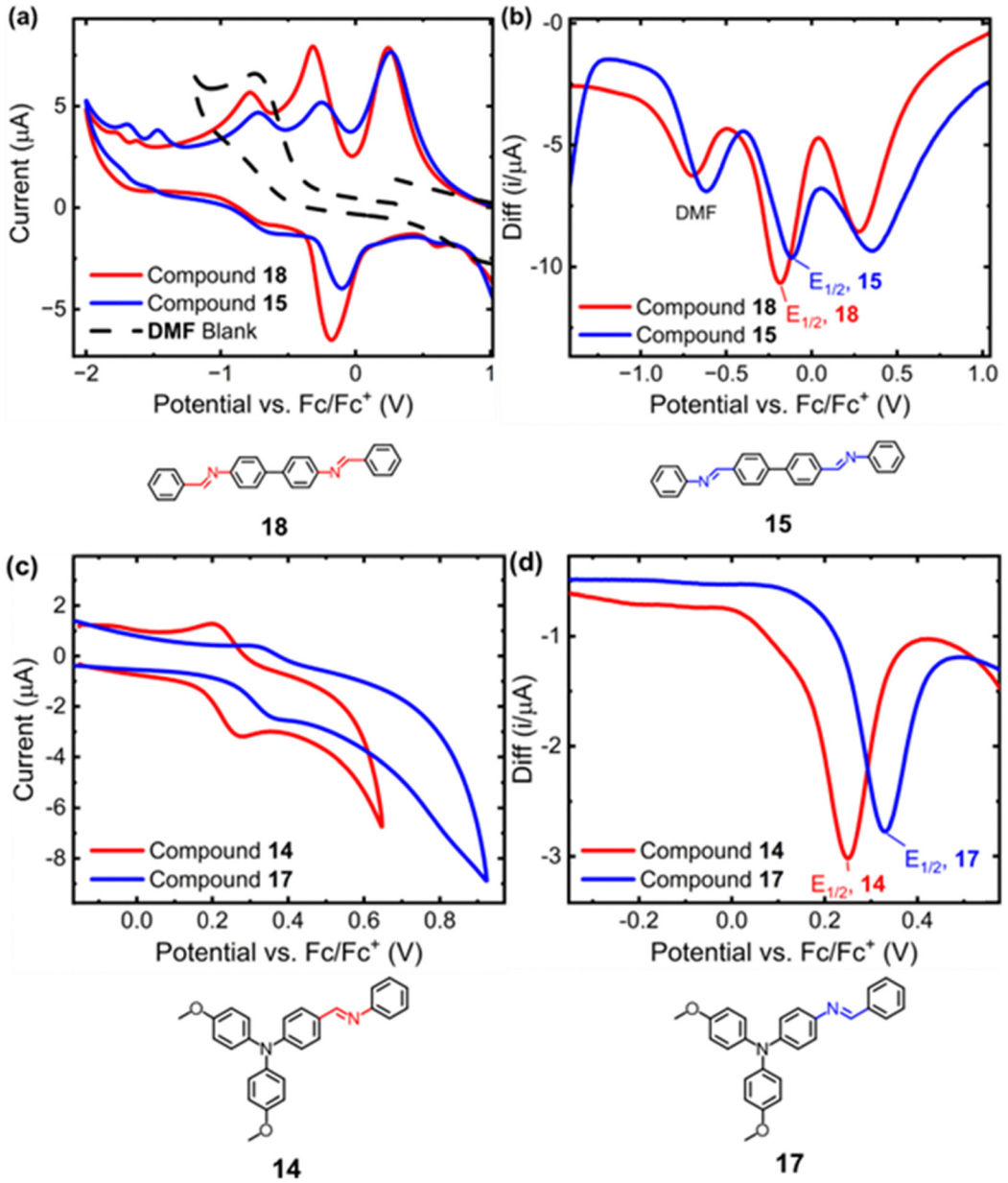

Fig. 6 (a) Overlaid CVs and (b) stacked SWVs of biphenyl model imines **18** and **15**. (c) Stacked CVs and (d) stacked SWVs of TPA-based model imines **17** and **14**. All voltammograms recorded from 10^{-4} M solutions in DMF.

Overall, the FTIR analysis revealed all expected bands that are characteristic of the organic functional groups in the investigated compounds. The theoretically predicted FT-IR spectra of both compounds (Fig. 9) show a similar profile to the experimental spectra. However, the predicted bands appear at slightly higher wavenumbers compared to those obtained experimentally, which is attributed to the gas phase calculations, which do not consider the intermolecular interactions.

Oxidation of HTMs and film conductivity

To gain insight into the chemical oxidation properties as well as the conductivities of compounds **10** and **12**, the materials were oxidised using different amounts of ionic oxidant FK209. Since the oxidation reaction with FK209 does not require oxygen as in the case of the well-known oxidant LiTFSI, FK209 was chosen to remove the need for ambiguous curing steps in a dry oxygen environment, thus standardising the experiments. FK209 is a cobalt based complex that oxidises the HTM through a redox reaction, generating a radical cation with the concomitant reduction of its Co(III) center to Co(II). Furthermore, FK209 does not result in hygroscopic byproducts being left in the film, as opposed to LiTFSI,[43] which is crucial for long-term device stability.

Fig. 10 shows the thin film UV-visible absorption spectra of compounds **10** and **12** treated with increasing concentrations of FK209. The growth of new peaks is observed in the absorption

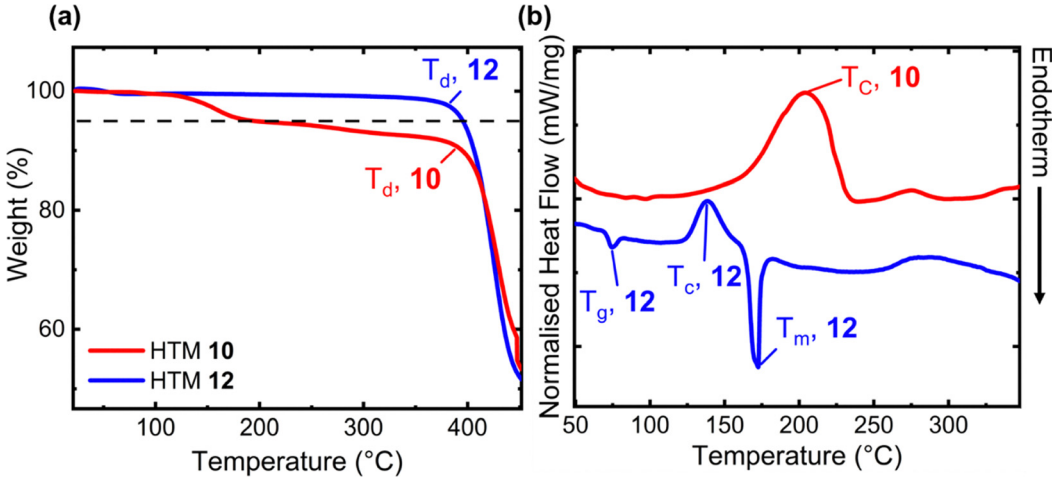

Fig. 7 (a) Overlaid TGA of compounds **10** and **12**. Dashed line represents 95% weight. (b) Stacked DSC thermograms of compounds **10** and **12**.

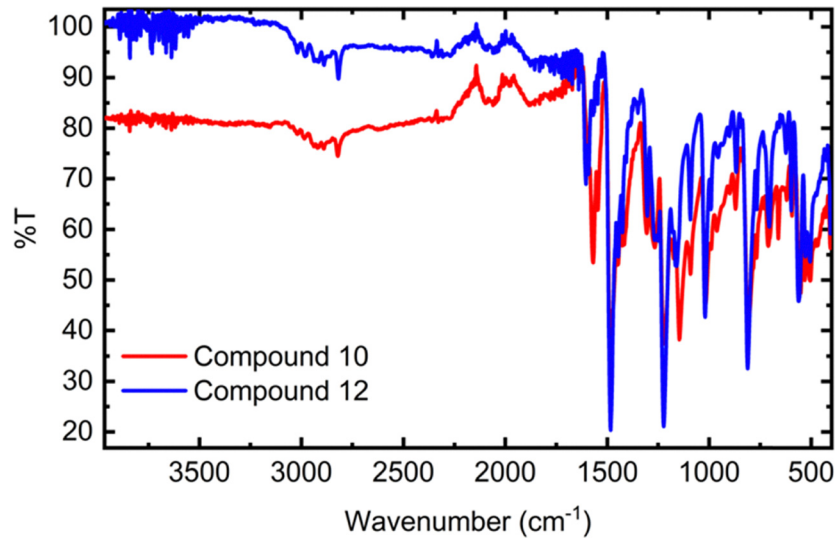

Fig. 8 Overlaid ATR-FTIR spectra for compounds **10** and **12**, measured experimentally on the neat solids.

profile upon addition of FK209, observed as an immediate colour change in solution, thus confirming a chemical reaction between HTM and oxidant. A large difference of ~255 nm is noted in the maximum absorbance of the oxidised species (λ_{ox}) for compound **10** and compound **12**, where the absorption of oxidised compound **12** occurs at much longer wavelengths compared to that of compound **10**. While the starting materials are isomeric, the oxidised products have vastly different optical band gaps and are likely to be very different chemical species. This suggests that the FK209 reactions proceed through very different pathways, despite both HTM solutions immediately exhibiting a colour change to dark red.

The conductivity of the imine-based HTMs oxidised with FK209 was also tested, since successful doping only occurs when mobile holes are generated in the oxidation reaction.[44] Interestingly, a notable difference in conductivity behaviour was observed for the two HTMs across the FK209 concentration range (Fig. 11). The conductivity of compound **10** showed a maximum increase of roughly an order of magnitude as opposed to compound **12**, which showed an increase by several orders of magnitude as the FK209 concentration was increased. The maximum conductivity obtained for compound **12** was in the order of 10^{-5} S cm^{-1} at 0.6 equivalents of FK209 oxidant. This indicates a significant decrease in doping efficiency for compound **10** compared to compound **12**, which was successfully doped by FK209, resulting in a substantial increase in conductivity. The conductivity of compound **10** does not increase even if the FK209 concentration in solution is increased to 1 equivalent, further emphasising the lack of doping. The low conductivity of compound **10** may be attributed either to insufficient hole mobility or negligible generation of extra holes, since the conductivity of holes in the film relies on both hole concentration and their mobility. Mobilities reported for similar HTMs were in the range of 10^{-5} cm^2 V^{-1} s^{-1},[27] suggesting that the newly

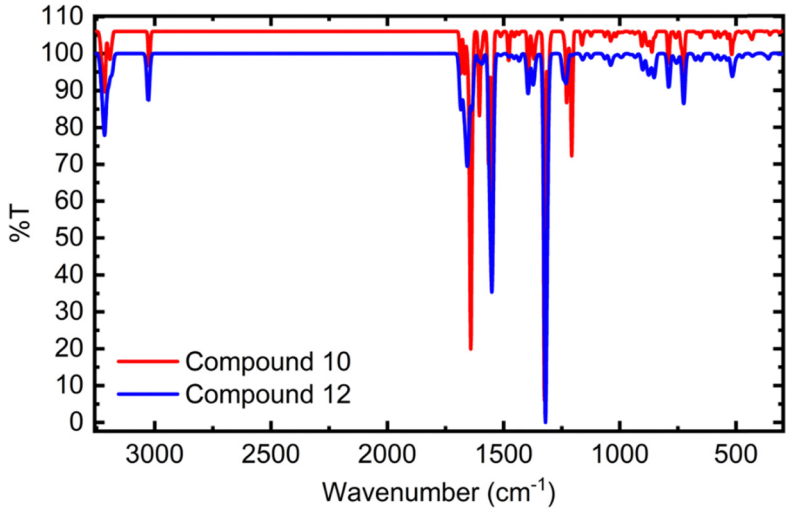

Fig. 9 Theoretically predicted gas-phase FTIR spectra for compounds **10** and **12**, calculated using density functional theory at the B3LYP 6-311G** level.

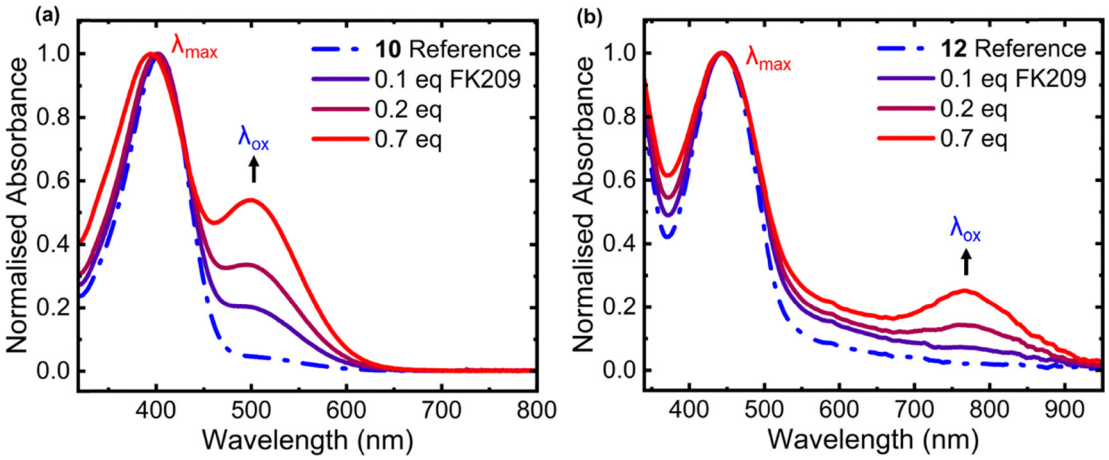

Fig. 10 Normalised thin film UV-visible absorption spectra of doped films of (a) compound **10** and (b) compound **12** recorded immediately after spin coating, with increasing concentration of FK209.

synthesized compounds in this work would be expected to exhibit comparable mobility values.

PSC fabrication

To show the practical utility of compounds **10** and **12**, we employed these molecules as HTMs for the fabrication of PSCs, using a configuration of FTO/c-TiO_2/SnO_2/$CsFAMAPbI_3$/HTM/Au, and measured their photovoltaic efficiency under one-sun illumination. We investigated the influence of the imine orientations on photovoltaic performance. PSCs were fabricated through solution spin coating, with the HTM solution containing HTM **10** or **12** at a concentration of 25 mM in chlorobenzene, as well as the additives LiTFSI, FK209, and *tert*-butylpyridine (*t*BP). The optimised recipe for the HTM solutions is detailed in the SI, Section S1.3. Compound **12** showed improved performance compared to compound **10** (Table 2 and Fig. 12). The low electrical conductivity of the two molecules resulted in poor fill factor (FF) and J_{sc}. Both the HTMs display a similar open circuit voltages (V_{oc}), suggesting identical band alignment, which follows the HOMO level calculations. The poor FF of devices fabricated with compound **10** is attributed to high series resistance resulting from reduced conductivity, and increased recombination, which creates shunting channels and inhibits hole collection. The significantly lower conductivity of compound **10** limits device performance due to ineffective transport of holes, highlighting the practical importance of imine bond orientations in optimising the device properties.

NMR and EPR analysis

From the results described above, it is clear that our two imine isomers **10** and **12** exhibit different oxidation behaviour. It is likely that compound **10** is unable to generate a mobile hole upon oxidation. In order to detect the generation of radical species, NMR and EPR spectroscopic methods were utilised. The initial stage in the process of doping involves the creation of radical cations within the HTM. It is possible to detect stable

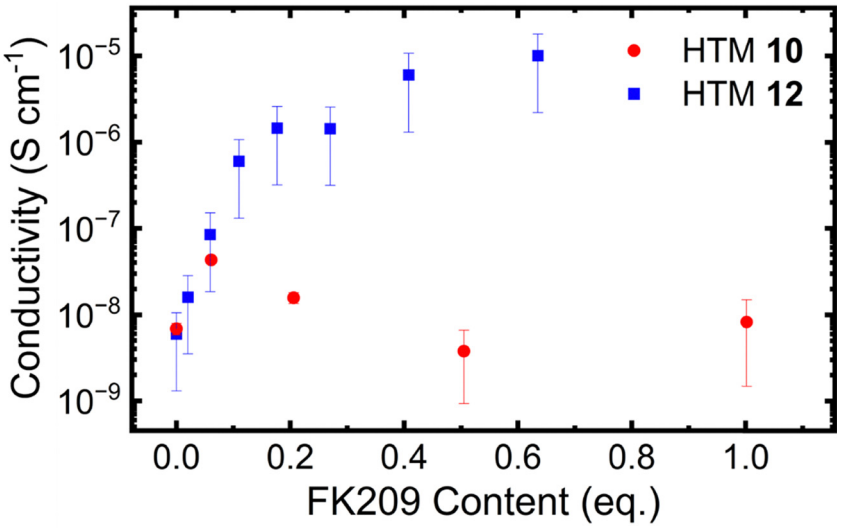

Fig. 11 Film conductivities of compounds **10** and **12**, with increasing FK209 concentration.

Table 2 Comparison of the champion photovoltaic device parameters for HTMs **10** and **12**

Compound	J_{sc} (mA cm^{-2})	V_{oc} (V)	FF	PCE (%)
12	14.9	0.89	62.33	8.2
10	0.7	0.85	13.88	0.1
Spiro-OMeTAD	23.8	1.04	73.55	18.2

radical species qualitatively through routine ^{1}H-NMR experiments since the interaction between unpaired electrons and NMR-active nuclei leads to the broadening of the NMR signals in the molecular regions that are involved, thus enabling qualitative detection of these radical species. This has been utilised in several studies for the oxidation of Spiro-OMeTAD.[45,46] EPR analysis can provide further insight by acting as a direct measurement of the presence of radical species which can confirm a successful doping reaction.

Fig. 13 shows the aromatic region of the ^{1}H-NMR spectrum of compounds **10** and **12**, as well as their corresponding AgTFSI-oxidised spectra. Two solutions of HTMs were prepared for NMR analysis, with the addition of one equivalent of AgTFSI to each solution. In this case, the utilisation of FK209 would introduce complexity to the analysis since the additive undergoes reduction to a paramagnetic Co(II) species. This Co(II) species would then contribute its paramagnetic broadening, thereby further complicating the analysis.[8] Thus, AgTFSI served as a strong chemical oxidising agent that was capable of generating HTM radicals without generating any byproducts in the reaction mixture. The only product formed was metallic

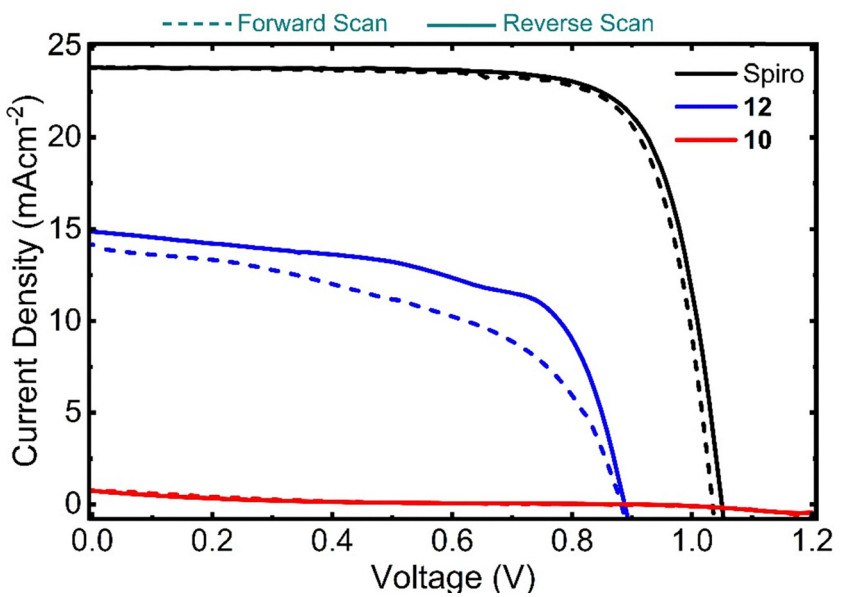

Fig. 12 *JV* characteristics of the champion devices fabricated with compounds **10**, **12**, and Spiro-OMeTAD (spiro) as the HTM.

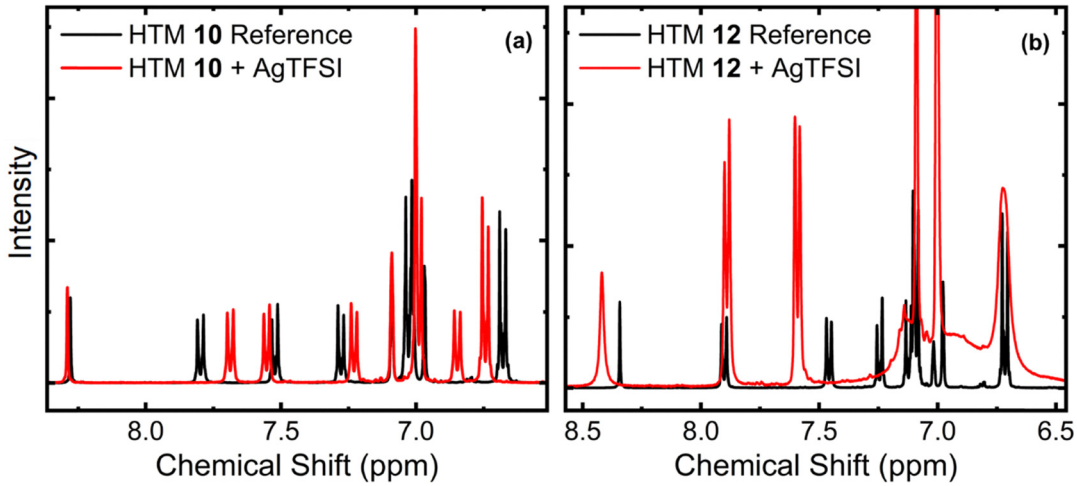

Fig. 13 The aromatic region of (a) compound **10** and (b) compound **12** ^{1}H-NMR spectra, recorded in toluene-d_8 before and after the addition of 1 equivalent of AgTFSI.

silver, which precipitated out of the solution and could be readily separated by filtration. AgTFSI readily oxidises both imine isomers as seen in the UV spectra in the SI, Fig. S14.

Fig. 13 illustrates that, upon the addition of AgTFSI, a change in the chemical shift of the aromatic proton signals in both HTMs is observed. Compound **12** shows a noticeable broadening in the aromatic region corresponding to the protons assigned to the TPA moiety, along with broadening of the imine proton signal (8.55 ppm). The observed signal broadening is likely due to the paramagnetic nature of the unpaired electron produced during the oxidation of AgTFSI. The peaks originating from the protons in the biphenyl core remain unchanged, indicating that the radical is entirely localised on the TPA arms.[45] On the other hand, there is no significant signal broadening observed for compound **10**, which might indicate that the interaction between compound **10** and AgTFSI results in side reactions that do not produce a detectable amount of radical species, hence supporting the lack of conductivity increase upon the addition of FK209 (Fig. 11).

EPR spectroscopy was then utilised to confirm the formation of radical species through the reaction of compounds **10** and **12** with AgTFSI (Fig. 14). This is essential since the conductivity of the HTM cannot be enhanced unless the species can stabilise the radical cation state. No EPR signals were observed for the control HTM solutions. However, when one equivalent of AgTFSI was added, a strong paramagnetic signal was observed for compound **12**, while compound **10** did not exhibit any evidence for radical formation, suggesting that it cannot sufficiently stabilise a radical cation. Consequently, this can further confirm the observed lack of conductivity increase upon the addition of FK209 for compound **10**. The NMR and EPR spectroscopic results confirm the electrochemical observations: the oxidation of compound **10** leads to an undesirable side reaction that fails to form a stable radical cation. It is possible

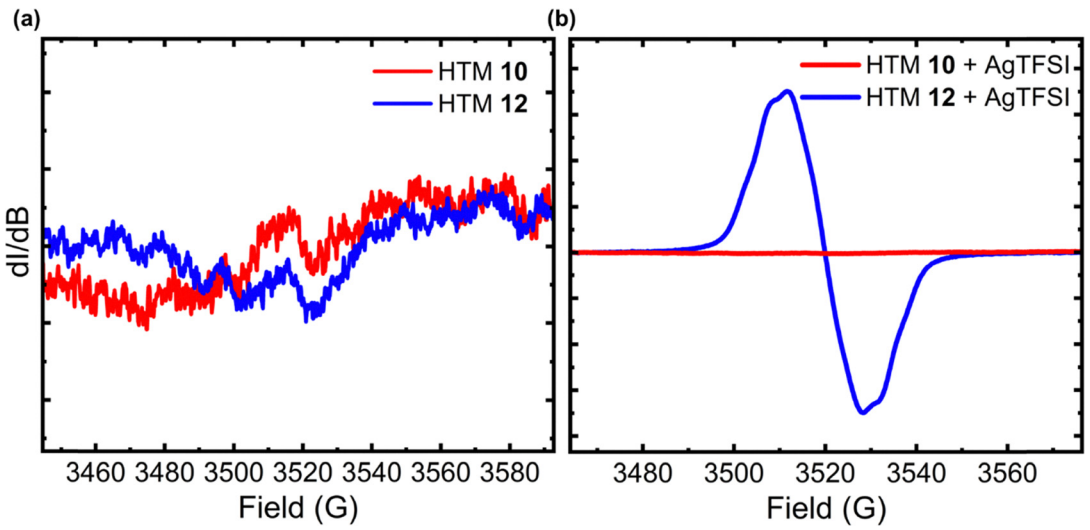

Fig. 14 (a) EPR spectra of undoped films of compounds **10** and **12**, (b) AgTFSI-doped films of compounds **10** and **12**.

that the oxidation of the core in compound **10** leads to an immediate quenching of the radical through a more energetically favourable mechanism.

Conclusion

We have developed hole transport materials with opposite imine bond orientations *via* facile condensation chemistry. The effect of the different imine orientations on materials doping and, therefore, oxidation mechanisms was then studied. Imine bond orientation has a substantial impact on the performance of materials in transferring holes, moreover, the orientation is closely connected to the oxidation mechanisms and conductivity. The difference in electron density distribution and consequent oxidation behaviour observed in the two orientations suggests the presence of competing oxidation pathways that impact the orientation over the other.

Following chemical oxidation, compound **12** showed the formation of stable and mobile holes, resulting in a considerable increase in film conductivity up to $\sim 10^{-5}$ S cm^{-1}. In contrast, compound **10** did not yield a significant hole concentration, thus limiting its utility and conductivity remained very low (10^{-8} S cm^{-1}). These observations are also reflected in the device properties. We highlight the importance of structure–function relationships in the molecular design and outline how simple alterations, such as the imine unit orientation, can significantly impact the efficiency of charge transport and device properties, thereby setting a guide towards the systematic design and the optimisation of future HTMs.

Conflicts of interest

The authors declare no conflict of interest.

Data availability

All data supporting the results of this study are available within the manuscript and its supplementary information (SI). Supplementary information: synthetic procedures, methodology for *J*–*V* and solar cell characterisation, NMR, FTIR, and mass spectrometry characterisation. See DOI: https://doi.org/10.1039/d6cp00309e.

Acknowledgements

This work was supported and funded by the Deanship of Scientific Research at Imam Mohammad Ibn Saud Islamic University (IMSIU) (grant number IMSIU-DDRSP2603). GC and DW thank the EPSRC (EP/V027425/1). GC also thanks the Leverhulme Trust for the award of a research fellowship. SA thanks the Spanish Ministry of Science and Innovation PHONON for funding (PID2024-163070OB-I00). PD acknowledges funding from the EPSRC under grant agreement EP/T010568/1 and the European Union's Marie Skłodowska-Curie Actions (MSCA) COFUND SmartBRAIN3 programme under grant agreement No 101126600.

References

1 X. Zhao and M. Wang, *Mater. Today Energy*, 2018, **7**, 208–220.
2 Shahnawaz, S. Sudheendran Swayamprabha, M. R. Nagar, R. A. K. Yadav, S. Gull, D. K. Dubey and J. H. Jou, *J. Mater. Chem. C*, 2019, **7**, 7144–7158.
3 A. Krishna and A. C. Grimsdale, *J. Mater. Chem. A*, 2017, **5**, 16446–16466.
4 N. Wang, J. Hu, L. Gao and T. Ma, *J. Electron. Mater.*, 2020, **49**, 7085–7097.
5 F. M. Rombach, S. A. Haque and T. J. Macdonald, *Energy Environ. Sci.*, 2021, **14**, 5161–5190.
6 L. M. Nhari, R. M. El-Shishtawy and A. M. Asiri, *Dyes Pigm.*, 2021, **193**, 109465.
7 S. Li, Y. L. Cao, W. H. Li and Z. S. Bo, *Rare Met.*, 2021, **40**, 2712–2729.
8 J. Burschka, A. Dualeh, F. Kessler, E. Baranoff, N. L. Cevey-Ha, C. Yi, M. K. Nazeeruddin and M. Grätzel, *J. Am. Chem. Soc.*, 2011, **133**, 18042–18045.
9 Y. Duan, Y. Chen, Y. Wu, Z. Liu, S. Liu and Q. Peng, *Adv. Funct. Mater.*, 2024, **34**, 2315604.
10 L. Nakka, Y. Cheng, A. G. Aberle and F. Lin, *Adv. Energy Sustainability Res.*, 2022, **3**, 2200045.
11 H. Chen, D. Bryant, J. Troughton, M. Kirkus, M. Neophytou, X. Miao, J. R. Durrant and I. McCulloch, *Chem. Mater.*, 2016, **28**, 2515–2518.
12 J. H. Chen, K. M. Lee, C. C. Ting and C. Y. Liu, *RSC Adv.*, 2021, **11**, 8879–8885.
13 L. Duan, Y. Chen, J. Yuan, X. Zong, Z. Sun, Q. Wu and S. Xue, *Dyes Pigm.*, 2020, **178**, 108334.
14 J. Salunke, X. Guo, Z. Lin, J. R. Vale, N. R. Candeias, M. Nyman, S. Dahlström, R. Österbacka, A. Priimagi, J. Chang and P. Vivo, *ACS Appl. Energy Mater.*, 2019, **2**, 3021–3027.
15 F. Zhang, Z. Wang, H. Zhu, N. Pellet, J. Luo, C. Yi, X. Liu, H. Liu, S. Wang, X. Li, Y. Xiao, S. M. Zakeeruddin, D. Bi and M. Grätzel, *Nano Energy*, 2017, **41**, 469–475.
16 H. Li, K. Fu, A. Hagfeldt, M. Grätzel, S. G. Mhaisalkar and A. C. Grimsdale, *Angew. Chem., Int. Ed.*, 2014, **53**, 4085–4088.
17 S. Paek, *Processes*, 2021, **9**, 2249.
18 D. Bi, B. Xu, P. Gao, L. Sun, M. Grätzel and A. Hagfeldt, *Nano Energy*, 2016, **23**, 138–144.
19 J. Jia, L. Duan, Y. Chen, X. Zong, Z. Sun, Q. Wu and S. Xue, *RSC Adv.*, 2019, **9**, 216–223.
20 E. Sheibani, L. Yang and J. Zhang, *Sol. RRL*, 2020, **4**, 2000461.
21 H. D. Pham, S. M. Jain, M. Li, Z. K. Wang, S. Manzhos, K. Feron, S. Pitchaimuthu, Z. Liu, N. Motta, J. R. Durrant and P. Sonar, *Adv. Electron. Mater.*, 2020, **6**, 1900884.
22 S. Lv, Y. Song, J. Xiao, L. Zhu, J. Shi, H. Wei, Y. Xu, J. Dong, X. Xu, S. Wang, Y. Xiao, Y. Luo, D. Li, X. Li and Q. Meng, *Electrochim. Acta*, 2015, **182**, 733–741.
23 E. A. A. Alkhudhayr, D. Sirbu, M. Fsadni, B. Vella, B. T. Muhammad, P. G. Waddell, M. R. Probert, T. J. Penfold,

T. Hallam, E. A. Gibson and P. Docampo, *ACS Appl. Energy Mater.*, 2023, **6**, 11573–11582.
24 M. L. Petrus, K. Schutt, M. T. Sirtl, E. M. Hutter, A. C. Closs, J. M. Ball, J. C. Bijleveld, A. Petrozza, T. Bein, T. J. Dingemans, T. J. Savenije, H. Snaith and P. Docampo, *Adv. Energy Mater.*, 2018, **8**, 1801605.
25 A. K. Pająk, P. Gnida, S. Kotowicz, J. G. Malecki, M. Libera, K. Bednarczyk and E. Schab-Balcerzak, *Energy Fuels*, 2020, **34**, 10160–10169.
26 K. A. Bogdanowicz, A. Iwan, K. Dysz, W. Przybyl, M. Marzec, K. Cichy and K. Świerczek, *Materials*, 2024, **17**, 1909.
27 M. L. Petrus, A. Music, A. C. Closs, J. C. Bijleveld, M. T. Sirtl, Y. Hu, T. J. Dingemans, T. Bein and P. Docampo, *J. Mater. Chem. A*, 2017, **5**, 25200–25210.
28 D. Vaitukaityte, Z. Wang, T. Malinauskas, A. Magomedov, G. Bubniene, V. Jankauskas, V. Getautis and H. J. Snaith, *Adv. Mater.*, 2018, **30**, 1803735.
29 D. H. Streater, E. R. Kennehan, D. Wang, C. Fiankor, L. Chen, C. Yang, B. Li, D. Liu, F. Ibrahim, I. Hermans, K. L. Kohlstedt, L. Luo, J. Zhang and J. Huang, *J. Am. Chem. Soc.*, 2024, **146**, 4489–4499.
30 D. Fan, R. Zhang, Y. Li, C. Shan, W. Li, Y. Wang, F. Xu, H. Fan, Z. Sun, X. Li, M. Zhao, A. K. K. Kyaw, G. Li, J. Wang and W. Huang, *Front. Chem.*, 2021, **9**, 1–11.
31 B. Cui, C. Zhu, S. Yang, Y. Han, N. Yang and L. Zhang, *ACS Omega*, 2018, **3**, 10791–10797.
32 M. L. Petrus, R. K. M. Bouwer, U. Lafont, S. Athanasopoulos, N. C. Greenham and T. J. Dingemans, *J. Mater. Chem. A*, 2014, **2**, 9474–9477.
33 M. L. Petrus, T. Bein, T. J. Dingemans and P. Docampo, *J. Mater. Chem. A*, 2015, **3**, 12159–12162.
34 D. Tsang, M. Bourgeaux and W. G. Skene, *J. Photochem. Photobiol., A*, 2007, **192**, 122–129.
35 M. Bourgeaux, S. A. P. Guarìn and W. G. Skene, *J. Mater. Chem.*, 2007, **17**, 972–979.
36 K. Suzuki, Y. Hori and T. Kobayashi, *Adv. Synth. Catal.*, 2008, **350**, 652–656.
37 J. Zeng, T. Zhang, X. Zang, D. Kuang, H. Meier and D. Cao, *Sci. China: Chem.*, 2013, **56**, 505–513.
38 J. P. Jeon, Y. J. Kim, S. H. Joo, H. J. Noh, S. K. Kwak and J. B. Baek, *Angew. Chem., Int. Ed.*, 2023, **62**, e202217416.
39 D. Sek, A. Iwan, B. Jarzabek, B. Kaczmarczyk, J. Kasperczyk, Z. Mazurak, M. Domanski, K. Karon and M. Lapkowski, *Macromolecules*, 2008, **41**, 6653–6663.
40 D. Alberga, G. F. Mangiatordi, F. Labat, I. Ciofini, O. Nicolotti, G. Lattanzi and C. Adamo, *J. Phys. Chem. C*, 2015, **119**, 23890–23898.
41 T. H. Schloemer, J. A. Christians, J. M. Luther and A. Sellinger, *Chem. Sci.*, 2019, **10**, 1904–1935.
42 J. Urieta-Mora, I. García-Benito, A. Molina-Ontoria and N. Martín, *Chem. Soc. Rev.*, 2018, **47**, 8541–8571.
43 A. Abate, T. Leijtens, S. Pathak, J. Teuscher, R. Avolio, M. E. Errico, J. Kirkpatrik, J. M. Ball, P. Docampo, I. McPherson and H. J. Snaith, *Phys. Chem. Chem. Phys.*, 2013, **15**, 2572–2579.
44 A. D. Scaccabarozzi, A. Basu, F. Aniés, J. Liu, O. Zapata-Arteaga, R. Warren, Y. Firdaus, M. I. Nugraha, Y. Lin, M. Campoy-Quiles, N. Koch, C. Müller, L. Tsetseris, M. Heeney and T. D. Anthopoulos, *Chem. Rev.*, 2022, **122**, 4420–4492.
45 T. Zhang, F. Wang, H.-B. Kim, I.-W. Choi, C. Wang, E. Cho, R. Konefal, Y. Puttisong, K. Terado, L. Kobera, M. Chen, M. Yang, S. Bai, B. Yang, J. Suo, S.-C. Yang, X. Liu, F. Fu, H. Yoshida, W. Chen, J. Brus, V. Coropceanu, A. Hagfelt, J.-L. Brédas, M. Fahlman, D. S. Kim, Z. Hu and F. Gao, *Science*, 2021, **377**, 495–501.
46 C. Geffroy, E. Grana, T. Bessho, S. Almosni, Z. Tang, A. Sharma, T. Kinoshita, F. Awai, E. Cloutet, T. Toupance, H. Segawa and G. Hadziioannou, *ACS Appl. Energy Mater.*, 2020, **3**, 1393–1401.